Article

Deep-Eutectic-Solvent-Assisted Synthesis of a Z-Scheme BiVO$_4$/BiOCl/S,N-GQDS Heterojunction with Enhanced Photocatalytic Degradation Activity under Visible-Light Irradiation

Hengxin Ren [1,2]✪, Kuilin Lv [3], Wenbin Liu [2], Pengfei Li [1], Yu Zhang [1] and Yuguang Lv [1,2,*]

1   College of Pharmacy, Jiamusi University, Jiamusi 154007, China
2   College of Materials Science and Engineering, Jiamusi University, Jiamusi 154007, China
3   China Building Materials Test and Certification Group Co., Ltd., Chaoyang District, Beijing100024, China
*   Correspondence: yuguanglv@163.com

Abstract: Z-scheme heterojunction photocatalytic nanomaterial designs have attracted attention due to their high catalytic performance. Deep eutectic solvents (DESs) have been used as green, sustainable media, acting as solvents and structure inducers in the synthesis of nanomaterials. In this work, a novel visible-light-absorption-enhanced bismuth vanadate/bismuth oxychloride/sulfur, nitrogen co-doped graphene quantum dot (BiVO$_4$/BiOCl/S,N-GQDS) heterojunction photocatalyst was prepared in a deep eutectic solvent. The photosynthetic activity of the BiVO$_4$/BiOCl/S,N-GQDS composite was determined by the photocatalytic degradation of rhodamine B (RhB) under visible-light irradiation. The results showed that the highest photocatalytic activity of BiVO$_4$/BiOCl/S,N-GQDS was achieved when the doping amount of S,N-GQDS was 3%, and the degradation rate of RhB reached 70% within 5 h. The kinetic and photocatalytic cycles showed that the degradation of Rhb was in accordance with the quasi-primary degradation kinetic model, and the photocatalytic performance remained stable after four photocatalytic cycles. Ultraviolet–visible diffuse reflectance (UV-DRS) and photoluminescence (PL) experiments confirmed that BiVO$_4$/BiOCl/S,N-GQDS ternary heterojunctions have a narrow band gap energy (2.35 eV), which can effectively improve the separation efficiency of the photogenerated electron–hole pairs and suppress their complexation. This is due to the construction of a Z-scheme charge process between the BiVO$_4$/BiOCl binary heterojunction and S,N-GQDS, which achieves effective carrier separation and thus a strong photocatalytic capability. This work not only provides new insights into the design of catalysts using a green solvent approach but also provides a reference for the study of heterojunction photocatalytic materials based on bismuth vanadate, as well as new ideas for other photocatalytic materials.

Keywords: BiVO$_4$; BiOCl; S; N-GQDS; heterojunction; photocatalysts

1. Introduction

In recent years, with population growth, sustained industrial development and economic globalization, human consumption of fossil energy has accelerated and released large quantities of organic and toxic pollutants into the natural environment, causing serious ecological damage. Traditional water control technology has the problems of cumbersome treatment methods and high application costs. Therefore, it is necessary to develop a practical, effective and environmentally friendly water treatment technology [1].

Since 1978, when J. H. Carey et al. used TiO$_2$ to catalyze the oxidative degradation of polychlorobiphenyls, photocatalysis has attracted a great deal of interest from researchers as an advanced technology for the oxidative degradation of pollutants [2]. Photocatalytic degradation based on semiconductor photocatalysts is deemed to be a very promising

technology for environmental remediation due to its energy savings, environmental friendliness and high degradation efficiency. In recent years, researchers have conducted many explorations to study the synthesis, application and catalytic mechanisms of semiconductor photocatalysts [3]. Nanosemiconductors, including $BiVO_4$, ZnS, CdS, Fe_2O_3, ZnO and Ag_2WO_4, have been used for a variety of environmental purifications, such as organic degradation, microbial inactivation and water splitting [4]. Despite their effectiveness, they suffer from e-/h+ recombination, wide-band-gap energy, and lower stability, all of which can significantly reduce their efficiency [5]. Therefore, some important techniques and modifications, such as the preparation of nanoparticles, doping and the construction of heterojunctions, have been applied to address these drawbacks [6].

N-type monoclinic crystalline $BiVO_4$ has attracted broad attention because of its narrow band gap (about 2.40 eV), so it has the advantages of visible-light-driven activity, a wide light absorption range and good photocatalytic performance. It is considered to be the most promising of the semiconductor photocatalytic reaction materials. It has been shown that $BiVO_4$ can better catalyze the degradation of organic pollutants under visible-light irradiation, but its photocatalytic degradation performance is limited due to the photogenerated carrier's low migration efficiency and fast recombination [7]. BiOCl is a p-type semiconductor material in which the chlorine atoms between the $[Bi_2O_2]$ layers are staggered along the c-axis to form a two-dimensional nano-layered structure, which facilitates the separation and transfer of the photogenerated carrier. However, due to the large band gap (about 3.5 eV), BiOCl absorbs less than 5 % of the UV light in sunlight and thus has poor photocatalytic performance under visible light [8]. It is worth noting that when a p-type semiconductor and an n-type semiconductor form a p-n heterojunction, an internal electric field will be formed between them, which accelerates the transfer of the photogenerated carrier and improves the separation efficiency of electron–hole pairs. This serves as a strategy to improve the activity of the $BiVO_4$ photocatalyst [9]. At present, $BiOCl/BiVO^4$ p-n heterojunction photocatalysts are synthesized by various methods, and their band gaps have been adjusted to increase their photoabsorption range and enhance their photocatalytic degradation capability for organic pollutants [10].

Sulfur–nitrogen-co-doped graphene (S,N-GQDS) has attracted much attention for its good biocompatibility, conductivity and photochemical properties [11]. These unique properties can be utilized to construct ternary heterojunctions with BiOCl and $BiVO_4$. When S,N-GQDS constructs a heterojunction with BiOCl and $BiVO_4$, it will be in close contact with BiOCl and $BiVO_4$. This will accelerate the interfacial charge transfer rate of the $BiVO_4$/BiOCl/S,N-GQDS heterojunction, reduce the impedance effect and enhance its photocatalytic properties. Fortunately, the structure of the ternary $BiVO_4$/BiOCl/S,N-GQDS heterojunction photocatalyst has not been reported [12].

The synthesis of a ternary heterojunction is usually difficult and requires expensive and even poisonous templates or surfactants, as well as strict synthetic conditions. A deep eutectic solvent (DES) is a kind of non-toxic, cheap and completely biodegradable organic solvent. By changing the charge neutralization, reduction potential or chemical activity, and passivation in a given crystal plane, the composition of the DES can modify the nucleation and growth mechanism of the crystal and thus determine its growth direction. Therefore, it is particularly suitable for the large-scale synthesis of novel functional materials, and as a pure green solvent, it is receiving more and more attention [13].

In summary, a novel $BiVO_4$/BiOCl/S,N-GQDS ternary heterostructure was prepared by the hydrothermal method with a deep eutectic solution as the solvent system. The photocatalytic degradation mechanism of the $BiVO_4$/BiOCl/S,N-GQDS heterojunction was evaluated using rhodamine B (RhB) as the model pollutant. This research is of great significance for solving the problem of water pollution.

2. Experimental Section

2.1. Photocatalyst Preparation

Preparation of bismuth vanadate: A mixture of choline chloride and urea (1:2) was heated at 70 °C for 30 min to produce 2 g of DES. One gram of distilled water was added to the solution to adjust its viscosity. Then, 0.01 mol $Bi(NO_3)_3 \cdot 5H_2O$ and 0.03 mol NH_4VO_3 were dissolved in 30 ml of DES and stirred by magnetic force for 1 h. The suspension was transferred to a 100 mL Teflon-lined stainless autoclave and heated at 180 °C for 5, 10 or 15 h. The product was cleaned repeatedly with deionized water and anhydrous ethanol, dried in a vacuum-drying box at 60 °C for about 12 h and kept in a Muffle Furnace at 500 °C for 2 h. The yellow $BiVO_4$ sample was finally obtained. In addition, 0.01mol $Bi(NO_3)_3 \cdot 5H_2O$ was added to a 100mL HCl solution (0.5 mol·L^{-1}) and ultrasonicated for 0.5 h. The reactants were placed in an autoclave and reacted at 180 °C for 15 h. BiOCl samples were obtained by the same cleaning and drying methods.

Preparation of S,N-GQD_S: First, 1.26 g of citric acid and 1.38 g of thiourea were dissolved in 30 mL of deionized water, stirred for 1 h to obtain a clear solution and then transferred to a 100 mL Teflon-lined stainless autoclave and heated at 180 °C for 8 h. The solution was cooled to room temperature and centrifuged at a speed of 10,000 rpm for 15 min. The precipitates were washed with deionized water and anhydrous ethanol (95%) several times and freeze-dried to obtain reddish-brown S,N-GQD_S solids.

The preparation of $BiVO_4/BiOCl/S,N$-GQD_S:1mmol $BiVO_4$ was dispersed in 10 mL of a HCl (0.5 mol L^{-1}) solution and stirred by magnetic force for 1 h. Then, precursors with different qualities were added and stirred for 0.5 h. The solution was transferred to a 25 mL Teflon-lined stainless-steel autoclave and heated at 180 °C for 10 h. The reaction products were washed with deionized water and ethanol many times and dried in a vacuum-drying box at 60 °C for 12 h. The samples were obtained and recorded as $BiVO_4/BiOCl/S,N$-GQD_S (1%), $BiVO_4/BiOCl/S,N$-GQD_S (3%) and $BiVO_4/BiOCl/S,N$-GQD_S (5%) according to the different mass fractions of S,N-GQD_S in the samples. In addition, $BiVO_4/BiOCl$ samples were obtained by using the same treatment method mentioned above without doping the precursors of S,N-GQD_S.

2.2. Photocatalytic Characterization

X-ray diffraction measurements were made by using a Bruker D8 Advance X-ray diffractometer (Bruker Aus, Germany) with Cu Kα radiation in the range $10° \leq 2\theta \leq 70°$. Fourier transform infrared (FT-IR) spectra were recorded on an IR Prestige-21 spectrometer (Shimadzu, Kyoto, Japan) using the KBr pellet technique at room temperature. An S-4700 Field Emission Scanning Electron Microscope (SEM; Hitachi Co., Japan) and a JEM-2010 transmission electron microscope (TEM; JOEL Ltd, Tokyo, Japan) were used to characterize the structure and morphology of the products. The light response ability of the sample was measured over a wavelength range of 800–200 nm on a UV-4100 UV-vis spectrophotometer (Shimadzu, Japan). The element composition and status of the sample were measured using X-ray photoelectron spectroscopy (Thermo ESCALAB 250XI, Thermo Fisher, Waltham, MA, USA). Photoluminescence (PL) spectra were measured using a Hitachi F-4600 fluorescence spectrophotometer (Hitachi, Tokyo, Japan) equipped with a 450 W Xenon lamp as the excitation source.

2.3. Evaluation of Photocatalytic Performance

The photocatalytic degradation of photocatalysts was evaluated by using rhodamine B as an organic dye model. First, 0.05 g of the photocatalyst sample was added to a 50 mL 10 mg·L^{-1} rhodamine B solution and stirred by magnetic force in the dark for 30 min. After the adsorption was balanced, a xenon lamp of 350 watts was irradiated as the visible light source. The absorption of a 5 mL solution was measured at intervals of 30 min. After centrifugation at high speed, the solution was purified, and the maximum absorption wavelength of 554 nm was determined by a UV-vis spectrophotometer. Finally, the solution

was poured back into the double beaker, and the reaction continued. The calculation method is given in Formula (1).

$$\text{Degradation rate of RhB} = \frac{C_t}{C_0} \times 100\% \qquad (1)$$

where C_0 indicates the initial mass concentration of RhB (mg·L^{-1}), and C_t represents the concentration of RhB at different times after photocatalytic degradation. After photocatalytic degradation, the photocatalyst solids were recovered. Subsequently, the photocatalyst was repeatedly cleaned with deionized water and anhydrous ethanol solution and vacuum-dried at 70 °C. Using the same photocatalytic degradation process, four experiments of photocatalytic degradation were carried out, and the X-ray diffraction patterns before and after photocatalytic degradation were compared to investigate the stability of the photocatalyst samples during photocatalytic degradation.

2.4. Evaluation of Photocatalytic Mechanism

The light absorption characteristics of the samples were studied by solid UV-Vis DRS. This method is used to analyze the displacement of the side band and the change in the forbidden band gap between them. The band gap of the sample can be calculated by the formula below.

$$\alpha h\upsilon = A\left(h\upsilon - E_g\right)^{n/2} \qquad (2)$$

where α is the absorption coefficient, $h\upsilon$ is the photon energy, A is a constant equal to 1, and E_g is the band-gap energy. The values of n are 4 for indirect transition and 1 for direct transition [14].

The valence- and conduction-band potentials of BiOCl and BiVO$_4$ can be calculated using their electronegativity with the following empirical equations.

$$E_{VB} = X + 0.5E_g - E_e \qquad (3)$$

$$E_{CB} = E_{VB} - E_g \qquad (4)$$

Here, E_{CB} and E_{VB} represent the conduction band edge and valence band edge, and E_g is the band-gap energy. X is the absolute electronegativity of the semiconductor, and E_e is a measurement scale factor of the redox level of the reference electrode relative to the absolute vacuum scale (-4.5 eV) [15].

In addition, the separation efficiency of photoelectrons and holes in visible-light samples was tested by photoluminescence (PL) spectroscopy. At the same time, iso-Propyl alcohol (IPA), p-Benzoquinone (BQ) and Ethylene Diamine Tetraacetic Acid (EDTA) were used as entrapment agents to detect the main reaction groups in the photocatalytic process.

3. Results and Discussion

3.1. Material Characterizations

As shown in Figure 1, all XRD characteristic diffraction peaks belong to BiVO$_4$ (JCPDS No. 83-1699) and BiOCl (JCPDS No. 73-2060), indicating the presence of BiOCl and BiVO$_4$ in the samples [16]. The diffraction peaks of S,N-GQDs are not obvious, mainly because of their instability in the HCl solution, resulting in a doping ratio lower than the theoretical value. In addition, there were no diffraction peaks of other substances in XRD mode, indicating the high purity of the prepared samples. The diffraction peaks at 2θ = 24.2° and 25.8° of the monoclinic BiVO$_4$ samples can be clearly observed when the processing times are 5 h and 10 h. These belong to BiOCl. Meanwhile, the diffraction peaks of the sample at 2θ = 18.6°, 18.9°, 28.5°, 28.8° and 30.5° can be observed. These peaks then belong to the monoclinic crystal system BiVO$_4$. This indicates that the sample is a mixture of BiOCl and monoclinic BiVO$_4$. After 15 h of treatment, the sample was in the monoclinic pyroxene BiVO$_4$ pure phase, crystallization was good, and the corresponding BiOCl diffraction peaks disappeared. This is due to hydrogen bonding between the hydroxyl group of choline

chloride and the polar group of urea, as well as unsaturated bonds and hydroxyl groups in the $BiVO_4$ crystal nucleus, which cause some solvent molecules to adsorb on the surface of $BiVO_4$, thus inducing the formation of BiOCl [17]. The characteristic peaks of $BiVO_4$ at $2\theta = 18.98°$ and $30.52°$ correspond to the {011} and {112} crystal planes, respectively. When $BiVO_4$ is recombined with BiOCl or S,N-GQDs, their intensity decreases noticeably, revealing that BiOCl and S,N-GQDs are favored to recombine with $BiVO_4$ on these two crystal planes. The crystallinity of the $BiVO_4$ sample decreased, and the half-peak width increased after compounding, which indicates that BiOCl and S,N-GQDs inhibit the growth of the monoclinic $BiVO_4$ crystal.
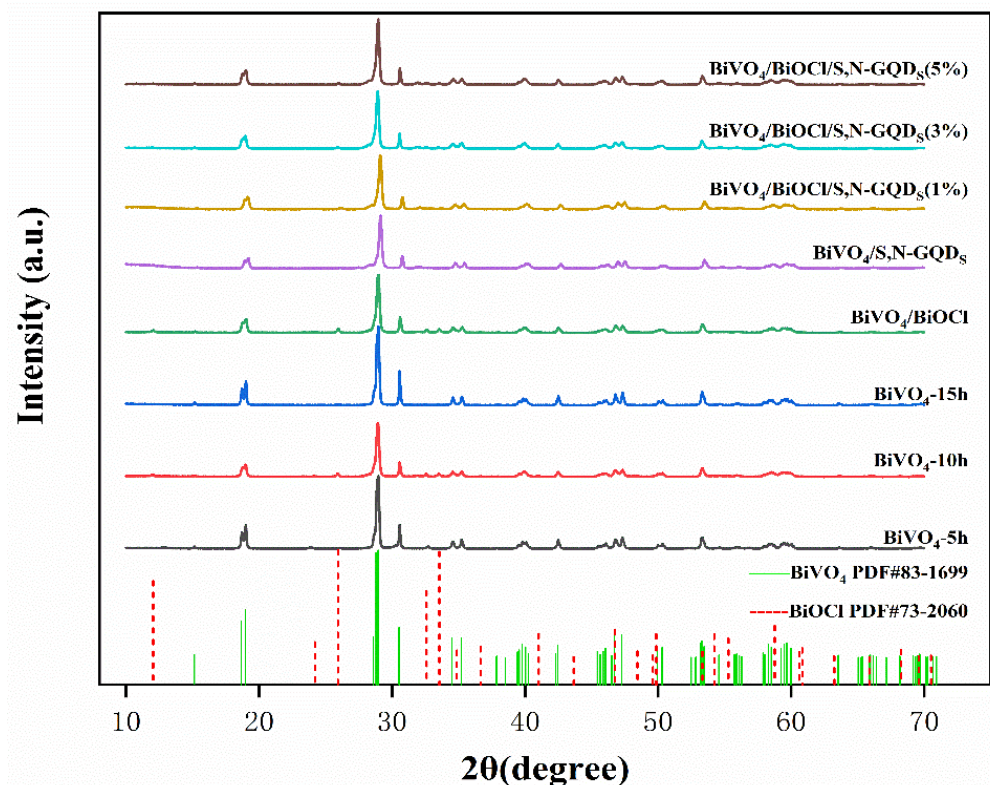

Figure 1. The XRD patterns of $BiVO_4$ samples with various treatment times, $BiVO_4$/BiOCl and $BiVO_4$/S,N-GQDs composites and $BiVO_4$/BiOCl/S,N-GQDs complex samples doped with different masses of S,N-GQDs.

As shown in the TEM image of the $BiVO_4$ sample in Figure 2A, the $BiVO_4$ sample is a block crystal. In Figure 2B, crystals in the $BiVO_4$/BiOCl composite sample can be found stacked and nested together. Figure 2C demonstrates that the distribution of S,N-GQDs is scattered without obvious aggregation. In Figure 2D, $BiVO_4$, BiOCl and S,N-GQDs are tightly bound together, from which different lattice stripes can be observed. The part with the lattice spacing of 0.374 nm is consistent with the {110} crystal plane and the lattice of BiOCl [18]. The part with the lattice spacing of 0.290 nm is attributed to the {011} crystal plane of $BiVO_4$, which is consistent with the XRD analysis [19]. In addition, the lattice spacing of S,N-GQDs is 0.241 nm, similar to the striations of the {1120} crystal plane of graphene [20]. This indicates that S,N-GQDs has the properties of graphene, which forms a ternary heterostructure together with the $BiVO_4$/BiOCl p-n heterojunction.
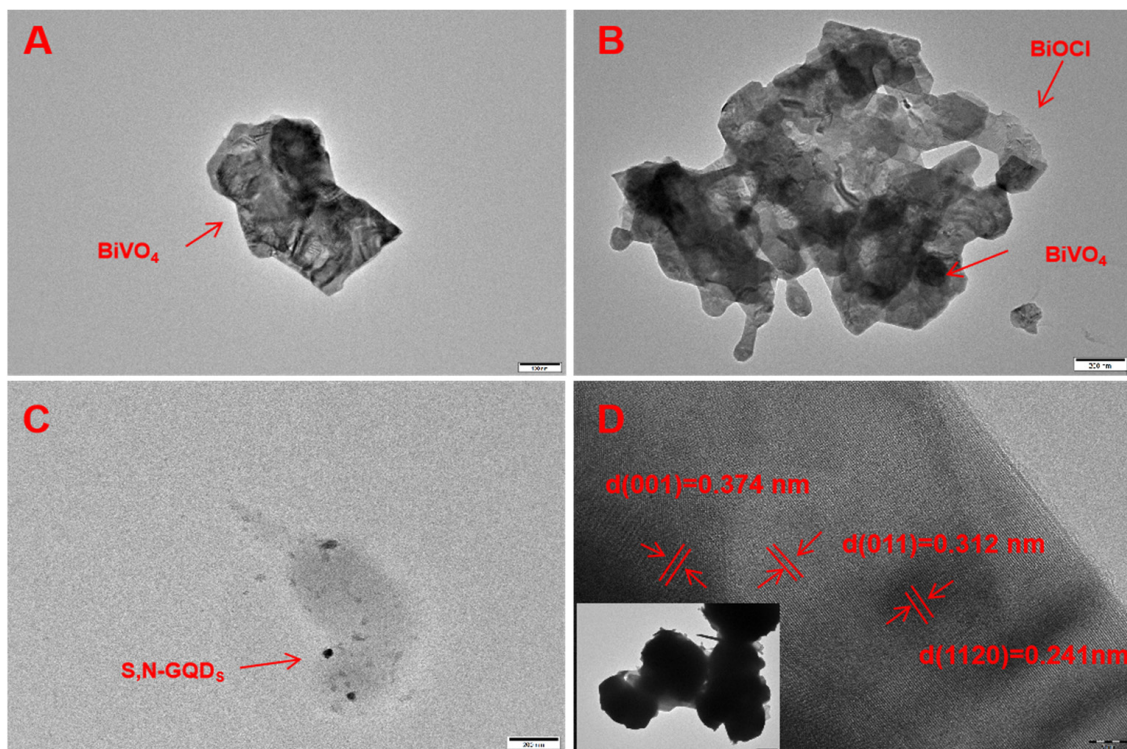
Figure 2. TEM images of BiVO$_4$ (**A**), BiVO$_4$/BiOCl (**B**) and S, N-GQD$_S$ (**C**); TEM and HRTEM of BiVO$_4$/BiOCl/S,N-GQD$_S$ functional composite nanomaterials (**D**).

It can be clearly observed from the SEM images that a large number of BiOCl nanosheets were attached to the surface of bulk BiVO$_4$ when the treatment time was 5 h (Figure 3A), while the BiOCl nanosheets gradually decreased when the treatment time was extended to 10 h (Figure 3B). Finally, when the treatment time reached 15 h, the BiOCl nanosheets disappeared, and only the pure-phase bulk BiVO$_4$ was retained (Figure 3C).
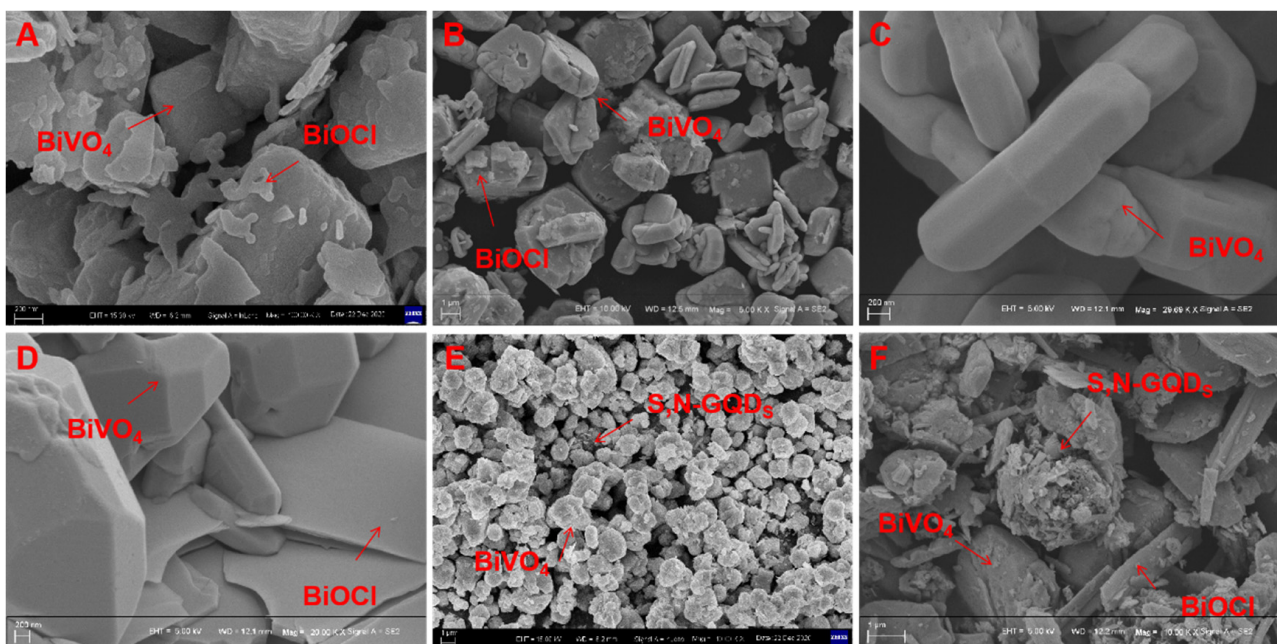

Figure 3. SEM images of BiVO$_4$ samples processed for different treatment times (**A**–**C**), BiVO$_4$/BiOCl (**D**), BiVO$_4$/S,N-GQD$_S$ (**E**) and BiVO$_4$/BiOCl/S,N-GQD$_S$ (**F**).

This is mainly due to the induction of the deep eutectic solution during the synthesis of $BiVO_4$, which can lead to the morphological evolution of $BiVO_4$ samples with the increase in retention time. The XRD characteristic analysis results confirm this phenomenon [21]. As seen in the SEM images (Figure 3D) of $BiVO_4/BiOCl$ samples with a high density of lamellar BiOCl and bulk $BiVO_4$ materials superimposed on each other, the formation of the $BiVO_4/BiOCl$ p-n heterojunction interface facilitates the transfer of photogenerated charges [22]. As shown in Figure 3E, in the $BiVO_4/S,N-GQD_S$ sample, a large amount of bulk $BiVO_4$ is visible, and only a small amount of spherical $S,N-GQD_S$ is distributed in it, which is related to the low doping of $S,N-GQD_S$. As shown in Figure 3F, the $BiVO_4/BiOCl/S,N-GQD_S$ sample consists of high-density BiOCl flakes and bulk $BiVO_4$ material stacked together, while $S,N-GQD_S$ are dispersed in it to assemble heterojunctions.

The EDS energy spectrum is shown in Figure 4, and the $BiVO_4/BiOCl/S,N-GQD_S$ (3%) composite contains Bi, O, V, S, N, C and Cl elements, further confirming the coexistence of $BiVO_4$, BiOCl and $S,N-GQD_S$. The calculated results show that the V:Cl atom percentage is 1:0.081, which is slightly lower than the theoretical mole ratio of 1:0.1. The Bi:(V+Cl) atomic percentage is 1.08:1, close to the theoretical value of the $BiVO_4/BiOCl$ complex of 1:1. The weight percentage of $BiVO_4:S,N-GQD_S$ is 1:0.026, which is close to the 3% doping ratio. The above results demonstrated that $BiVO_4/BiOCl/S,N-GQD_S$ (3%) were synthesized successfully.
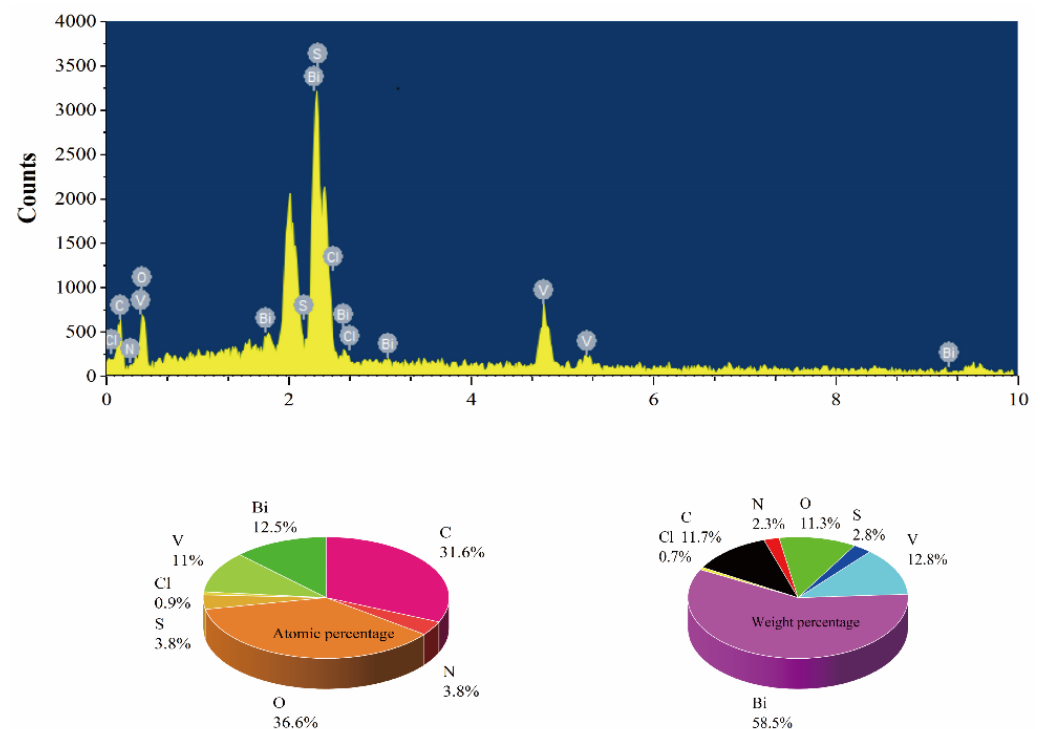

Figure 4. EDS energy spectrum of $BiVO_4/BiOCl/S,N-GQD_S$ (3%) sample.

Figure 5A shows the full spectrum of the X-ray photoelectron spectra of $BiVO_4/BiOCl/S,N-GQD_S$ (3%) photocatalyst samples. It consists of Bi, V, Cl, O, S, N and C elements with atomic mass percentages of 5.15, 3.57, 1.17, 30.01, 0.31, 4.52 and 55.27, respectively. Figure 5A shows the X-ray photoelectron spectroscopy results of samples of the $BiVO_4/BiOCl/S,N-GQD_S$ (3%) photocatalyst. It includes Bi, V, Cl, O, S, N and C elements with atomic mass percentages of 5.15, 3.57, 1.17, 30.01, 0.31, 4.52 and 55.27, respectively. The calculated atomic percentage of bismuth:(V/Cl) is 1.09:1, which is close to the theoretical 1:1 value of the $BiVO_4/BiOCl$ complex. This is consistent with the results of the EDS analysis. In Figure 5B, the XPS spectrum of C1s shows a dominant peak at a binding energy of 284.95 eV, which is attributed to C-C due to sp2 hybridization. In addition, there are two characteristic peaks

of lower intensity. The characteristic peak with a binding energy of 286.65 eV belongs to C-N, C-S and C-O due to sp3 hybridization. The characteristic peak with a binding energy of 288.65 eV belongs to C=O in carbonyl and carboxylates [23]. As shown in Figure 5C, the characteristic peaks of binding energies at 529.5 eV, 531.8 eV and 533.2 eV are high-resolution XPS signals of O 1s, corresponding to Bi-O and absorbed oxygen on the composite surface, respectively [24]. The two strong peaks of binding energies at 164.2 eV and 159.0 eV in Figure 5D are Bi 4f5/2 and Bi 4f7/2, respectively, which are characteristic peaks of Bi^{3+}. This indicates that the type of bismuth in the samples of $BiVO_4$/BiOCl/S,N-GQD$_S$ (3%) is Bi^{3+}. The characteristic peaks of V^{5+} at 516.1 and 523.8 eV in Figure 5E are attributed to V 2p3/2 and V 2p1/2, respectively. The characteristic peaks of Cl 2p3/2 and Cl 2p1/2 can be observed at 197.8 eV and 199.4 eV (Figure 5F) [25]. The XPS signals of N1s can be seen at 398.5, 400.8 and 402.2 eV, attributed to imine ($=N^-$), amine (-NH-) and protonated imine ($=NH^+$), respectively. In addition, the S2p spectrum in Figure 5H clearly shows the characteristic peak of S^{2-} at 224.63 eV. The presence of the characteristic peaks of S2p and N1s confirms that S and N elements were successfully doped into GQD$_S$ [26]. The coexistence of $BiVO_4$, BiOCl and S,N-GQD$_S$ in the composite was further confirmed by XPS, XRD and SEM.

The Fourier transform infrared spectroscopy (FT-IR) spectrum of the sample is shown in Figure 6. Absorption peaks at 512 cm^{-1} all appear due to the stretching vibration of Bi-O, while the absorption peak at 742 cm^{-1} belongs to the bending vibration of $v3$ (VO$_4$). The wavelength near 1622 cm^{-1} belongs to the stretching vibrational band of C-O in the -COOH and -CONH groups of S,N-GQD$_S$ [27]. The distinct vibrational peak at 3459 cm^{-1} corresponds to the O-H stretching vibration of the water molecule. Due to the small doping amounts of S and N elements and the strong stretching vibration of VO_4^{3-} and Bi-O, there are no obvious C-N and C-S absorption peaks [28]. In summary, it can be concluded that $BiVO_4$/BiOCl/S,N-GQD$_S$ composites contain Bi-O and VO_4^{3-} groups.

3.2. Photodegradation Properties

Under simulated-natural-light irradiation, rhodamine B dye was used as the target contaminant for degradation. The photocatalytic degradation activities of $BiVO_4$ samples prepared with different holding times, namely, $BiVO_4$/BiOCl, $BiVO_4$/S,N-GQD$_S$ complexes and $BiVO_4$/BiOCl/S,N-GQD$_S$ complex samples with different doping masses of S,N-GQD$_S$, were analyzed. In order to accurately determine the concentration of rhodamine B solution, the standard curve of the rhodamine B (RhB) solution was established using different concentrations of rhodamine B standard solutions, and the regression equation and correlation coefficient R^2 were obtained by linear fitting. As shown in Figure 7A, the equation of the standard curve of the rhodamine B (RhB) solution was: y = 0.2015x − 0.0312, and R^2 = 0.9991, indicating that the equation was quite linear and could be used for the determination of the rhodamine B solution concentration. The photocatalytic degradation curves of each sample are shown in Figure 7B. The photocatalytic degradation rates in order of strength to weakness within 5 h are: $BiVO_4$/BiOCl/S,N-GQD$_S$ (3%) (85%) > $BiVO_4$/BiOCl/S,N-GQD$_S$ (1%) (81%) > $BiVO_4$/BiOCl/S,N-GQD$_S$ (5%) (78%) > $BiVO_4$/BiOCl (62%) > $BiVO_4$/S,N-GQD$_S$ (59%) > $BiVO_4$-10h (55%) > $BiVO_4$-15h (46%) > $BiVO_4$-5h (40%). To quantitatively describe the rate of the catalytic reaction, the kinetic fitting of the reaction of the material to degrade the target contaminant was performed by fitting the above degradation curve with the Langmuir–Hinshelwood equation. The calculation method is shown in Equation (5).
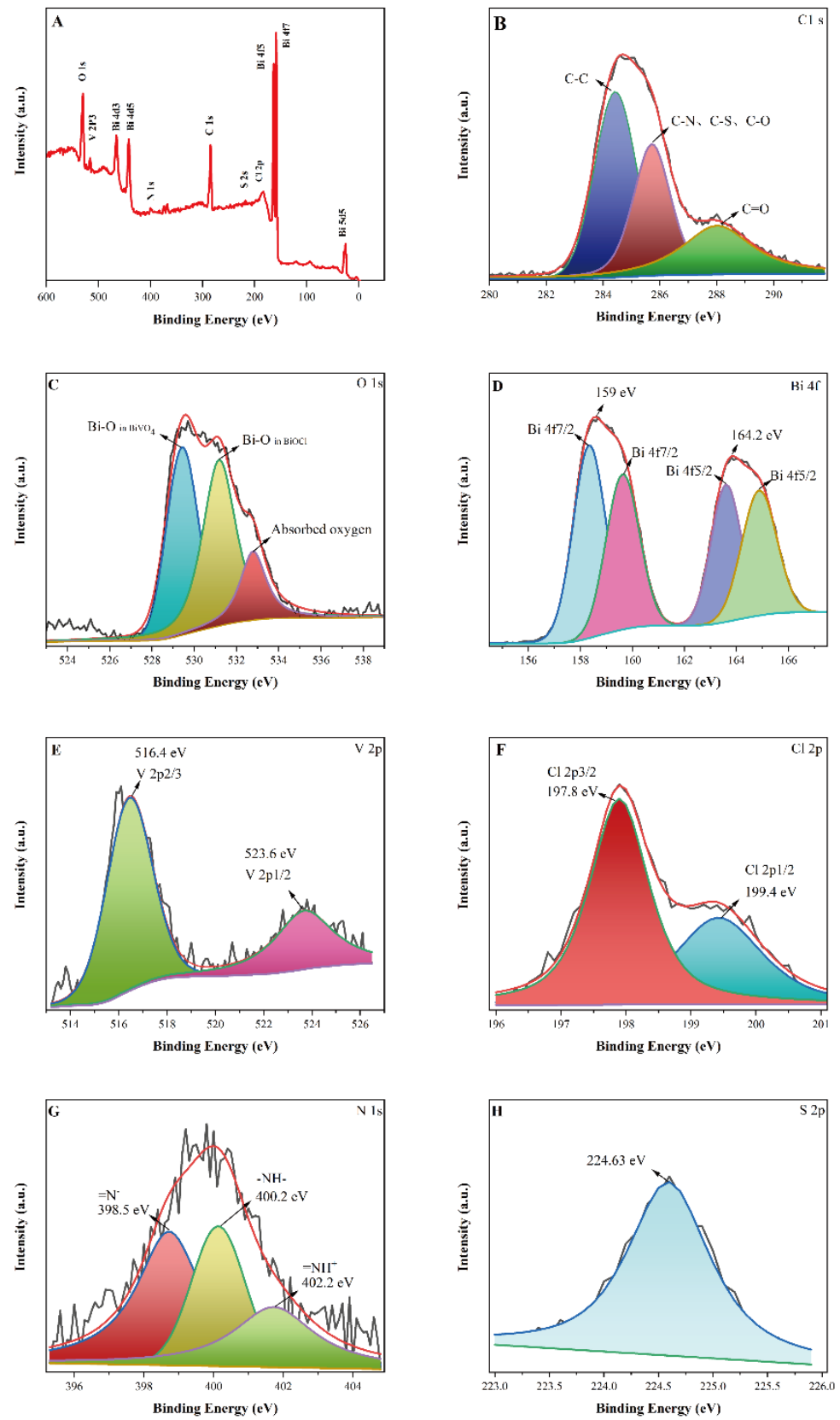
Figure 5. XPS patterns of BiVO$_4$/BiOCl/S,N-GQD$_S$ samples: full spectrum (**A**), C 1s (**B**), O 1s (**C**), Bi 4f (**D**), V 2p (**E**), Cl 2p (**F**), N 1s (**G**) and S 2p (**H**).
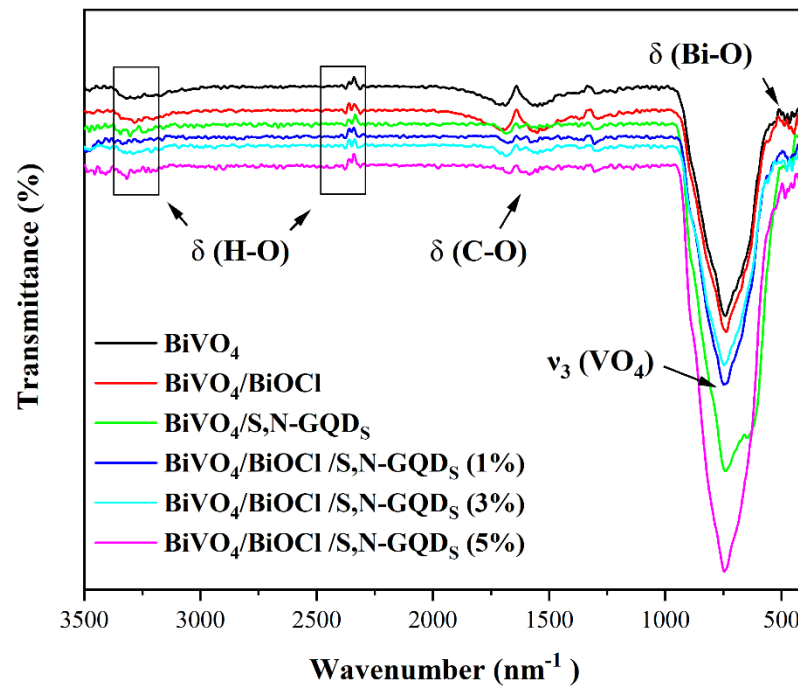
Figure 6. FT-IR spectra of $BiVO_4$, $BiVO_4/BiOCl$, $BiVO_4/S,N\text{-}GQD_S$ and $BiVO_4/BiOCl/S,N\text{-}GQD_S$ complex samples doped with different masses of $S,N\text{-}GQD_S$.

$$\ln(C_0/C_t) = kt \tag{5}$$

where ln is the natural logarithm, and *K* is the photodegradation reaction constant. A larger value of *K* means better photocatalytic activity of the sample. In addition, C_0 is the initial concentration of the RhB dye, and C_t is the RhB concentration at reaction time t. As shown in Figure 7C, the reaction rate constants for different preservation times (5, 10 and 15 h), $BiVO_4/BiOCl$, $BiVO_4/S,N\text{-}GQD_S$ complexes and $BiVO_4/BiOCl/S,N\text{-}GQD_S$ were 0.1565, 15657, 160.47, 130.475, 240.377, 240.377 and 0.267, respectively. Meanwhile, the correlation coefficients for linear fits, R^2, were determined to be 0.9582, 0.97061, 0.9756, 0.99341, 0.98718, 0.98754, 0.99045 and 0.98347. The information in Figure 7B,C shows that the degradation rates of $BiVO_4$ samples with a holding time of 15 h are lower than those with a holding time of 5 or 10 h. This is due to the $BiVO_4$ sample containing a small amount of BiOCl at a 5 h or 10 h holding time, thus forming a P-n heterojunction with $BiVO_4$, so the effect of catalytic degradation is greater than that of the pure phase of $BiVO_4$. The heterostructure of $BiVO_4$ with BiOCl or $S,N\text{-}GQD_S$ can significantly improve the photocatalytic degradation, among which $BiVO_4/BiOCl/S,N\text{-}GQD_S$ (3%) can obtain the best photocatalytic degradation performance. Figure 7D shows the spectra of 3% $BiVO_4/BiOCl/S,N\text{-}GQD_S$ samples at different degradation times. The results showed that, with the prolongation of the degradation time, the absorption value of the RhB solution gradually decreased, the maximum absorption spectra were blue-shifted, and a new absorption peak was produced at 515 nm. This is due to the reaction of RhB with the photocatalyst, which removes a portion of the ethyl groups and generates a new product [29].
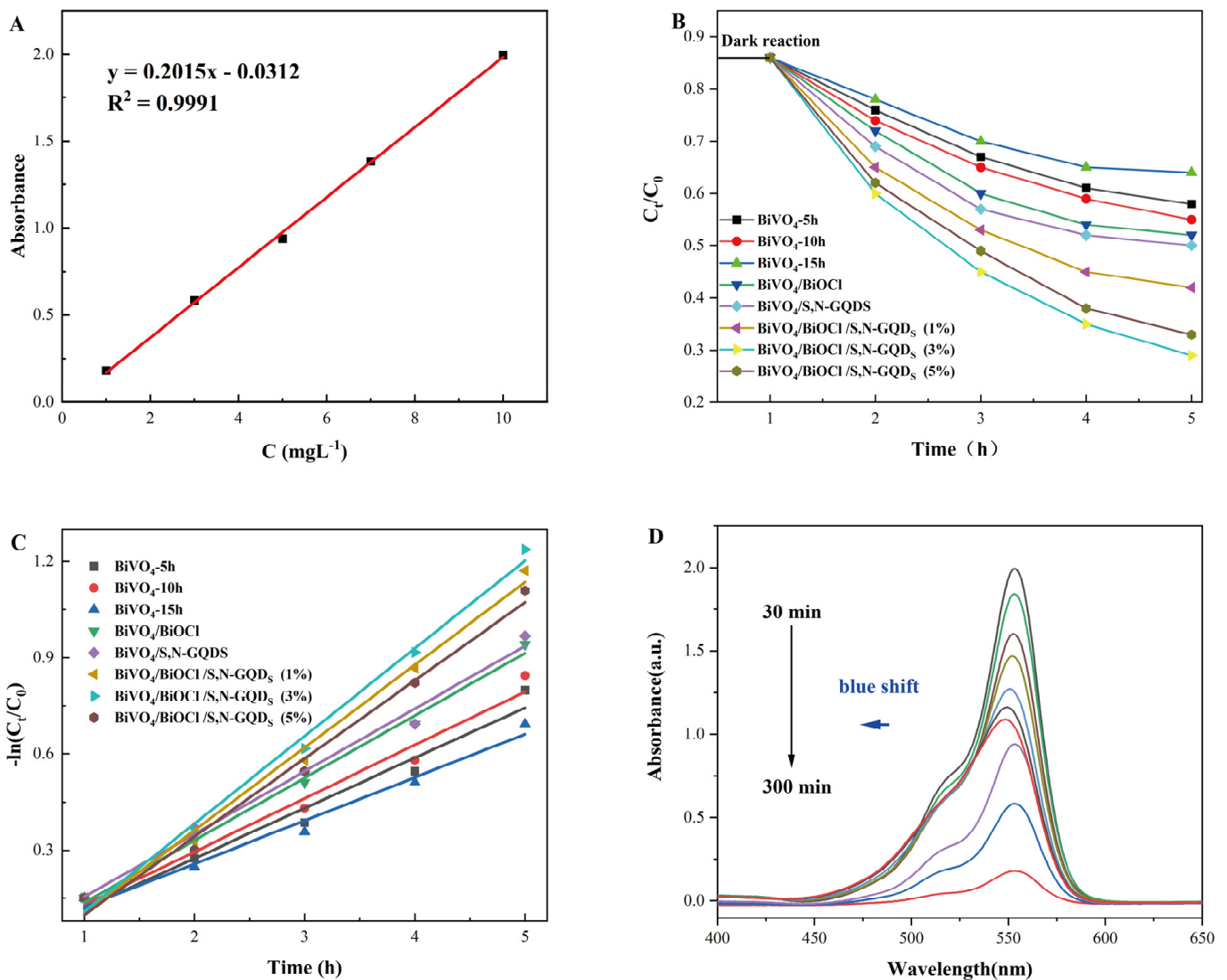
Figure 7. Experimental results of photocatalytic degradation: (**A**): standard curve of rhodamine B (RhB) solution; (**B**): photocatalytic degradation curve of prepared samples; (**C**): kinetic study of the sample in the degradation of RhB; (**D**): UV absorption spectrum of rhodamine B degraded by the $BiVO_4/BiOCl/S,N\text{-}GQD_S$ (3%) sample.

The stability and reproducibility of the experimental results for the photocatalytic degradation of $BiVO_4/BiOCl/SN\text{-}GQDs$ (3%) catalyst samples are shown in Figure 8. After four photocatalytic cycles, the photocatalytic activity of the $BiVO_4/BiOCl/S,N\text{-}GQDs$ (3%) photocatalyst sample was still high, and the crystal structure was still monoclinic scheelite without any change. This indicates that the $BiVO_4/BiOCl/S,N\text{-}GQDS$ (3%) photocatalyst samples do not undergo photocorrosion during the photocatalytic degradation of RhB and have good stability and reproducibility. The comparative analysis of the performance of the prepared $BiVO4/BiOCl/S,N\text{-}GQDS$ samples with other bivo4-based heterojunctions for the degradation of RhB shows that the degradation performance of the prepared $BiVO4/BiOCl/S,N\text{-}GQDS$ samples is superior, as shown in Table 1.
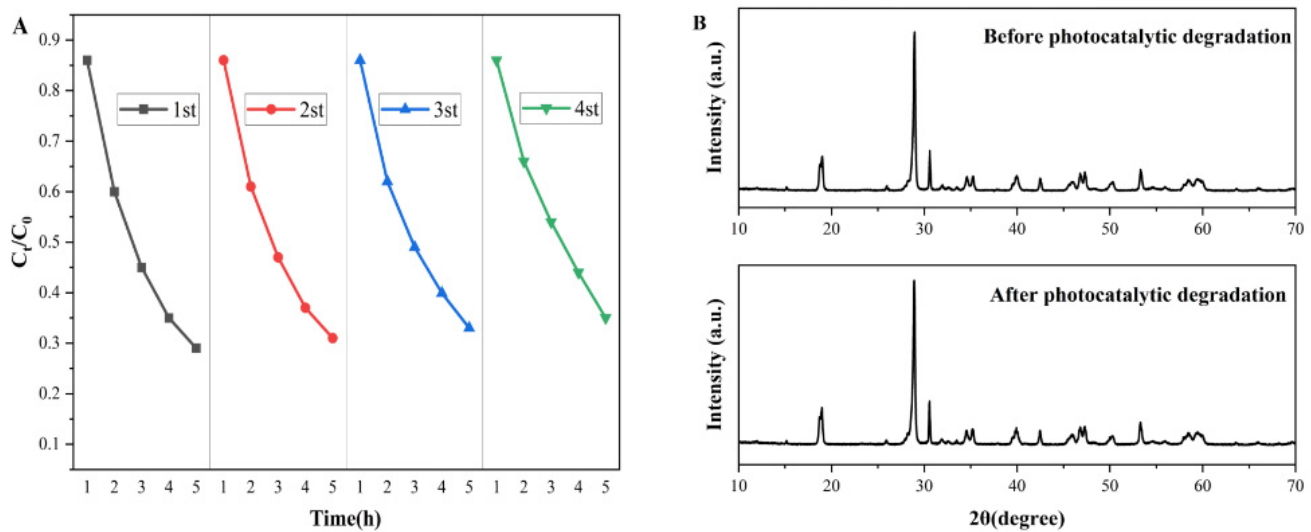
Figure 8. Photostability test plots of the cyclic photocatalytic degradation of RhB by the BiVO$_4$/BiOCl/S,N-GQD$_S$ sample (**A**) and XRD patterns before and after photocatalytic cycling experiments (**B**).

Table 1. Comparison of degradation performance of RhB by bivo$_4$ based heterojunction.

Sample	$m_{photocatalyst}$:m_{RhB}	Illumination Source	Degradation Rate/Time	Reference
BiVO$_4$	208:1	Halogen Lamp (500 W)	97.7%/6 h	[30]
BiVO$_4$/BiOCl	125:1	Xenon Lamp (500 W)	93%/210 min	[31]
BiVO$_4$/BiOCl/WO$_3$	150:1	Xenon Lamp (350 W)	75%/3 h	[32]
BiVO$_4$/TiO$_2$	208:1	Xenon Lamp (350 W)	62%/6 h	[33]
BiVO$_4$/BiOCl/S,N-GQD$_S$	100:1	Xenon Lamp (350 W)	85%/5 h	-

3.3. Photocatalytic Mechanism

Figure 9A shows the UV–visible diffuse reflectance spectra of the prepared photocatalyst. BiOCl has a light absorption threshold of 310 nm in the UV region. The light absorption threshold of BiVO$_4$ and its composite sample was shifted to 500 nm in the visible-light region, indicating the redshift of the sample's absorption edge after heterojunction formation. As shown in Figure 9B, the forbidden band gap of the BiOCl, BiVO$_4$, S,N-GQD$_S$, BiVO$_4$/BiOCl, BiVO$_4$/S,N-GQD$_S$, BiVO$_4$/BiOCl/S,N-GQD$_S$ (1%), BiVO$_4$/BiOCl/S,N-GQD$_S$ (3%) and BiVO$_4$/BiOCl/S,N-GQD$_S$ (5%) samples were 3.36, 2.41, 2.1, 2.42, 2.36, 2.38, 2.35 and 2.37 eV, respectively. According to the energy-band theory, the forbidden bandwidth determines the photoresponse range of semiconductor photocatalysts. Obviously, the BiVO$_4$/BiOCl/S,N-GQD$_S$ (3%) sample has the narrowest forbidden band gap (2.35 eV), so it can utilize more sunlight and enable more photogenerated carriers to separate and transfer, thus improving the photocatalytic performance. The X values for BiOCl and BiVO$_4$ are about 6.35 eV and 6.03 eV, respectively. Using Equations (3) and (4), the values of E_{VB} and E_{CB} of BiOCl were calculated to be 3.53eV and 0.17 eV, while the E_{VB} and E_{CB} values of BiVO$_4$ were 2.74 eV and 0.33 eV, respectively [34]. The E_{CB} of S,N-GQD$_S$ was determined by XPS to be -0.8 eV, and the E_{VB} of S,N-GQDS was calculated to be 1.3 eV using Equation (4).
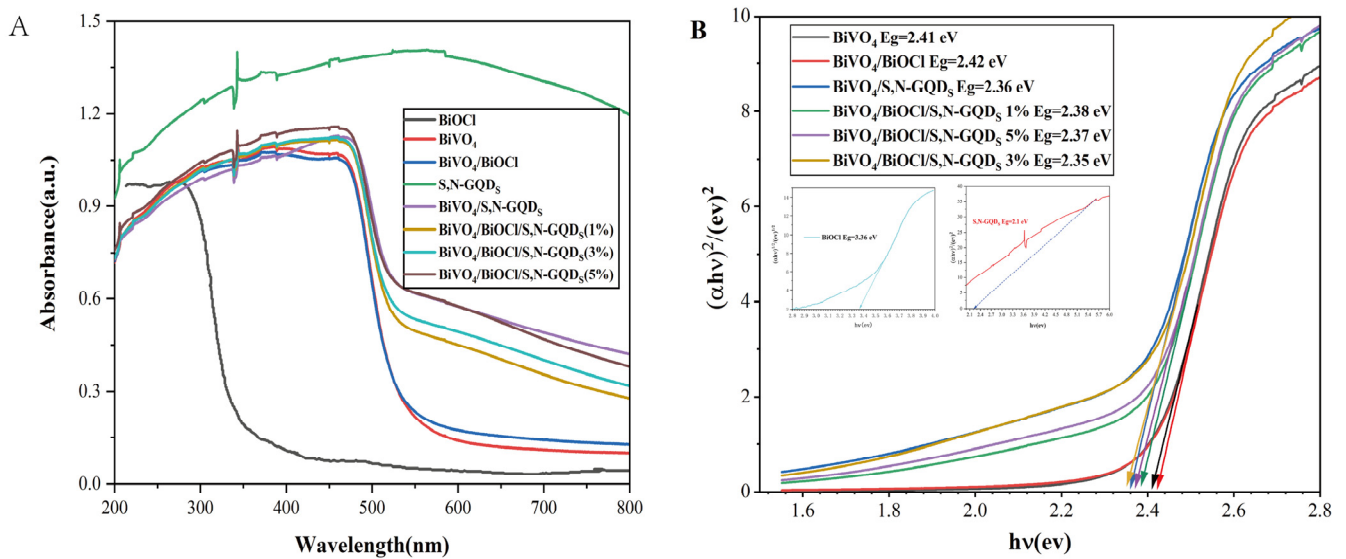
Figure 9. UV-vis diffuse reflectance spectra of different samples (**A**) and band-gap energy (**B**).

The photoluminescence spectra of $BiVO_4$ and its heterojunction photocatalysts are shown in Figure 10, which shows that the photoluminescence spectra of all samples have similar shapes, with emission peaks near 495 and 530 nanometers, respectively. In addition, the decreasing order of the PL peak intensities of these samples is as follows: $BiVO_4$-10h > $BiVO_4$/BiOCl > $BiVO_4$-5h > $BiVO_4$/BiOCl/S,N-GQD$_S$ (5%) > $BiVO_4$-15h > $BiVO_4$/BiOCl/S,N-GQD$_S$ (1%) > $BiVO_4$/S,N-GQD$_S$ (3%) > $BiVO_4$/BiOCl/S,N-GQD$_S$ (3%). Obviously, the PL emission peak intensity of the $BiVO_4$/BiOCl/S,N-GQD$_S$ (3%) sample is the lowest, which suggests that the construction of the $BiVO_4$/BiOCl/S,N-GQD$_S$ (3%) ternary heterojunction can effectively decrease the chance of electron and hole complexation through photogeneration.
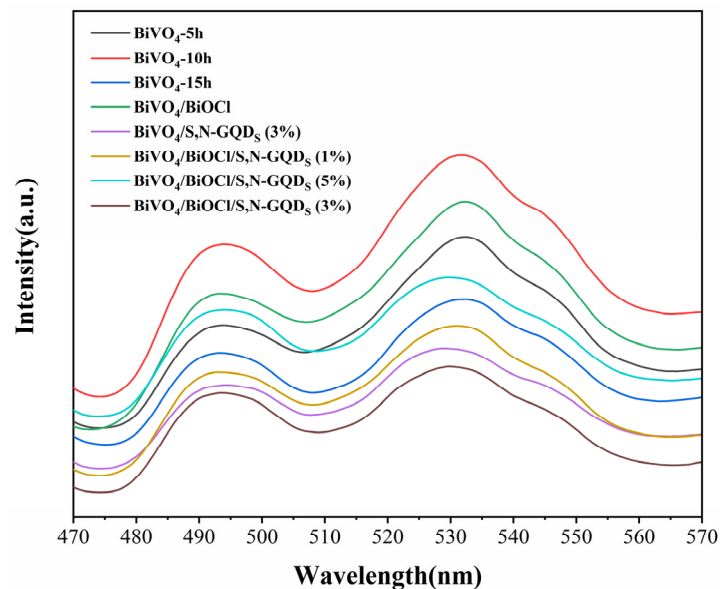

Figure 10. The PL spectrum of $BiVO_4$ samples after different treatment times: $BiVO_4$/BiOCl and $BiVO_4$/S,N-GQD$_S$ composites and $BiVO_4$/BiOCl/S,N-GQD$_S$ complex samples doped with different masses of S,N-GQD$_S$.

The results of active-group-capture experiments for the photocatalytic degradation of RhB by $BiVO_4/BiOCl/S,N\text{-}GQD_S$ (3%) samples are shown in Figure 11, and it can be found that the addition of EDTA has almost no effect on the performance of the photocatalytic degradation of RhB, but the performance of the photocatalytic degradation of RhB after adding p-benzoquinone and IPA under the same conditions decreased from 85% to 40% and 44% within 300 min, respectively. This indicates that the photocatalytic degradation of RhB in the prepared photocatalytic materials is not performed by the h^+ reaction group but by the $\bullet OH$ and $\bullet O^{2-}$ reaction groups.
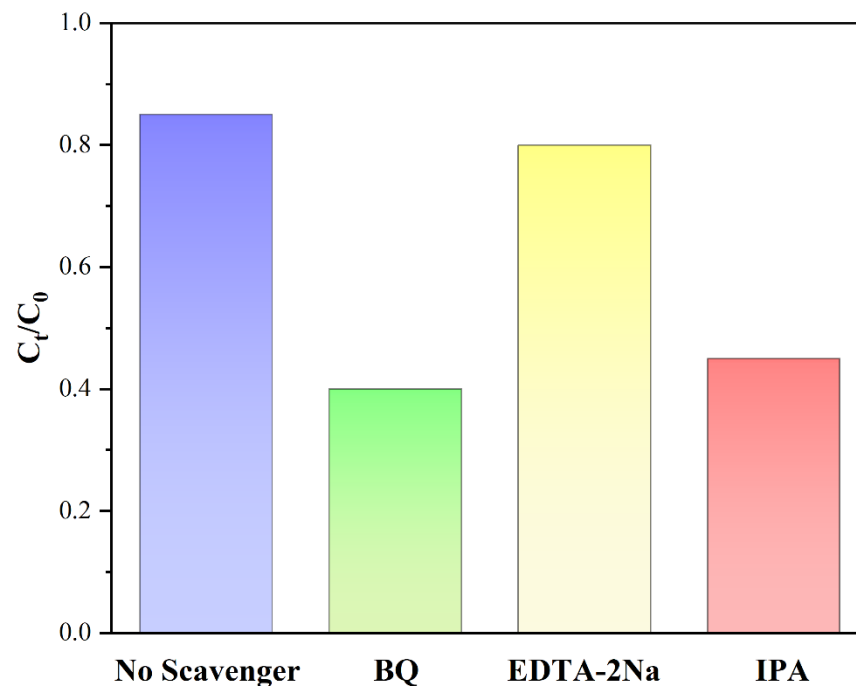

Figure 11. The results of the reactive-group-capture experiment for the photocatalytic degradation of RhB by the $BiVO_4/BiOCl/S,N\text{-}GQD_S$ (3%) sample.

Based on the above experimental results, Figure 12 introduces in detail the separation and transfer process of the $BiVO_4/BiOCl/S,N\text{-}GQD_S$ ternary-heterojunction-photogenerated carrier and its possible photocatalytic degradation mechanism. Since the band gaps of $BiVO_4$ and $S,N\text{-}GQD_S$ are narrow, they can be excited simultaneously under visible-light irradiation. In contrast, BiOCl cannot be excited to produce photogenerated carriers because of its wide band gap. However, this situation changes after the construction of the $BiOCl/BiVO_4/N\text{-}GQDs$ ternary heterojunction. When BiOCl and $BiVO_4$ are tightly bonded together, the p-type BiOCl and n-type $BiVO_4$ form a $BiOCl/BiVO_4$ p-n heterojunction [35]. Meanwhile, an internal electric field is formed at their interface, which can provide a potential driving force to promote electron transfer from the VB of BiOCl to the VB of $BiVO_4$, resulting in the generation of holes (h+) in the VB of BiOCl, while no electrons can be generated in the CB of BiOCl. The VB of BiOCl (2.4 eV) is more positive than the redox potential of $\bullet OH/OH^-$ (2.38 eV), so h^+ can oxidize OH^- to $\bullet OH$ [36]. Because $S,N\text{-}GQD_S$ has both p-type and n-type semiconductor characteristics [37], when $BiVO_4$ and $S,N\text{-}GQD_S$ are tightly bound together, the e^- in the CB of $BiVO_4$ recombines with the h^+ in the VB of $S,N\text{-}GQD_S$ through a Z-scheme charge transfer process. This eventually leads to more e^- and h^+ remaining in the CB of $S,N\text{-}GQD_S$ and in the VB of $BiVO_4$, respectively. The CB of $S,N\text{-}GQD_S$ (−0.80 eV) is more negative than the redox potential of $O_2/\bullet O^{2-}$ (−0.046 eV), so e- can reduce O_2 to $\bullet O^2$. The oxidative degradation of RhB can be achieved by large amounts of -OH and $\bullet O^{2-}$. On the other hand, RhB consumes more $\bullet O^{2-}$ and $\bullet OH$ during its degradation by photocatalytic oxidation, which induces more electron transfer and generates more e^- and h^+, and so on and so forth until the degradation process is finished.
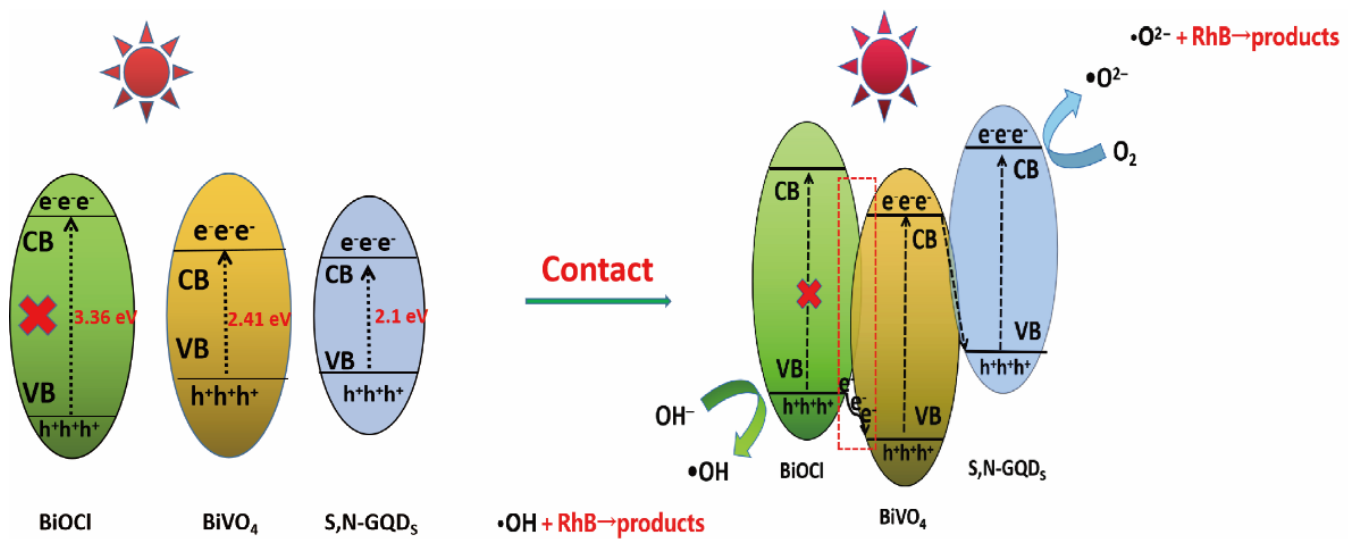
Figure 12. Schematic diagram of the mechanism of photocatalytic degradation of RhB by $BiVO_4/BiOCl/S,N-GQD_S$ samples.

4. Conclusions

A novel visible-light-absorption-enhanced $BiVO_4/BiOCl/S,N-GQD_S$ ternary heterojunction photocatalyst was successfully prepared, and a tentative mechanism to explain the significantly enhanced photoactivity was proposed. The photocatalyst's catalytic degradation of RhB experimentally proved that the construction of a Z-scheme heterogeneous structure is one of the effective strategies to improve the catalytic activity of the photocatalyst. The highest photocatalytic activity was achieved when the $S,N-GQD_S$ doping amount was 3%, and the RhB degradation rate could reach 81%. Moreover, the samples remained stable after four cycles of degradation. The formation of heterojunctions can promote electron transfer and inhibit the complexation of electron–hole pairs, which can significantly improve the photocatalytic activity of pure $BiVO_4$. The formation of heterojunctions promotes electron transfer and inhibits the complexation of electron–hole pairs, enhancing the effects of the radicals $\bullet O^{2-}$ and $\bullet OH$. Meanwhile, the smaller forbidden band gap (2.35 eV) improves the efficiency of visible-light utilization, which can significantly improve the photocatalytic activity of pure $BiVO_4$. The economy and environmental friendliness of the solution were improved by the use of deep eutectic solvents. In addition, the issue of how to improve the recovery rate of the material during practical applications while improving the photocatalytic performance of the material is also worthy of our consideration.

Author Contributions: Conceptualization, H.R. and Y.L.; methodology, H.R.; software, W.L.; validation, K.L. and P.L.; formal analysis, Y.Z.; investigation, H.R.; resources, Y.L.; data curation, H.R.; writing—original draft preparation, H.R.; writing—review and editing, H.R. and Y.L.; visualization, P.L.; supervision, W.L.; project administration, Y.L.; funding acquisition, Y.Z. All authors have read and agreed to the published version of the manuscript.

Conflicts of Interest: The authors declare no conflict of interest.

References

1.　Alharbi, N.S.; Hayat, T.; Rabah, S.O.; Alsaedi, A.; Zhuang, L.; Wang, X. Efficient elimination of environmental pollutants through sorption-reduction and photocatalytic degradation using nanomaterials. *Front. Chem. Sci. Eng.* **2020**, *14*, 1124–1135. [CrossRef]

2.　Carey, J.H.; Lawrence, J.; Tosine, H.M. Photodechlorination of PCB's in the presence of titanium dioxide in aqueous suspensions. *Bull. Environ. Contam. Toxicol.* **1976**, *16*, 697–701. [CrossRef] [PubMed]

3.　Zhang, X.; Wang, J.; Dong, X.-X.; Lv, Y.-K. Functionalized metal-organic frameworks for photocatalytic degradation of organic pollutants in environment. *Chemosphere* **2019**, *242*, 125144. [CrossRef] [PubMed]

4.　Ren, H.; Qin, Y.; Lv, Y. Preparation and Photocatalytic Activity of Novel PPy/GO/BiVO$_4$ Nanocomposites. *Surf. Rev. Lett.* **2022**, *29*, 2250009. [CrossRef]

5.　Khan, S.H.; Pathak, B. Zinc oxide based photocatalytic degradation of persistent pesticides: A comprehensive review. *Environ. Nanotechnol. Monit. Manag.* **2020**, *13*, 100290. [CrossRef]

6.　Jabbar, Z.H.; Ebrahim, S.E. Recent advances in nano-semiconductors photocatalysis for degrading organic contaminants and microbial disinfection in wastewater: A comprehensive review. *Environ. Nanotechnol. Monit. Manag.* **2022**, *17*, 100666. [CrossRef]

7.　Liu, L.; Hu, T.; Dai, K.; Zhang, J.; Liang, C. A novel step-scheme BiVO$_4$/Ag$_3$V$_4$ photocatalyst for enhanced photocatalytic degradation activity under visible light irradiation. *Chin. J. Catal.* **2021**, *42*, 46–55. [CrossRef]

8.　Antonatos, N.; Kovalska, E.; Mazánek, V.; Veselý, M.; Sedmidubský, D.; Wu, B.; Sofer, Z. Electrochemical exfoliation of Janus-like BiTeI nanosheets for electrocatalytic nitrogen reduction. *ACS Appl. Nano Mater.* **2021**, *4*, 590–599. [CrossRef]

9.　Meng, S.; Ogawa, T.; Okumura, H.; Ishihara, K.N. The effect of potassium chloride on BiVO$_4$ morphology and photocatalysis. *J. Solid State Chem.* **2021**, *302*, 122291. [CrossRef]

10.　Feng, C.; Wang, D.; Jin, B.; Jiao, Z. The enhanced photocatalytic properties of BiOCl/BiVO$_4$ p–n heterojunctions via plasmon resonance of metal Bi. *RSC Adv.* **2015**, *5*, 75947–75952. [CrossRef]

11.　Ma, C.; Din, S.T.U.; Seo, W.C.; Lee, J.; Kim, Y.; Jung, H.; Yang, W. BiVO$_4$ ternary photocatalyst co-modified with N-doped graphene nanodots and Ag nanoparticles for improved photocatalytic oxidation: A significant enhancement in photoinduced carrier separation and broad-spectrum light absorption. *Sep. Purif. Technol.* **2021**, *264*, 118423. [CrossRef]

12.　Saravanakumar, K.; Park, C.M. Rational design of a novel LaFeO$_3$/g-C$_3$N$_4$/BiFeO$_3$ double Z-scheme structure: Photocatalytic performance for antibiotic degradation and mechanistic insight. *Chem. Eng. J.* **2021**, *423*, 130076. [CrossRef]

13.　Zhang, Q.; De Oliveira Vigier, K.; Royer, S.; Jérôme, F. Deep eutectic solvents: Syntheses, properties and applications. *Chem. Soc. Rev.* **2012**, *41*, 7108–7146. [CrossRef] [PubMed]

14.　Verma, P.; Samanta, S.K. Continuous ultrasonic stimulation based direct green synthesis of pure anatase-TiO$_2$ nanoparticles with better separability and reusability for photocatalytic water decontamination. *Mater. Res. Express* **2018**, *5*, 065049. [CrossRef]

15.　Zhou, Z.; Li, Y.; Lv, K.; Wu, X.; Li, Q.; Luo, J. Fabrication of walnut-like BiVO$_4$@ Bi$_2$S$_3$ heterojunction for efficient visible photocatalytic reduction of Cr(VI). *Mater. Sci. Semicond. Process.* **2018**, *75*, 334–341. [CrossRef]

16.　Maheskumar, V.; Jiang, Z.; Lin, Y.; Bhojan, V.; Sasikumar, S. Synergistic effect of Ag and Cu co-doping on the structural, optical, and photocatalytic performance of BiVO$_4$. *J. Mater. Sci. Mater. Electron.* **2021**, *32*, 23811–23824. [CrossRef]

17.　Liu, W.; Yu, Y.; Cao, L.; Su, G.; Liu, X.; Zhang, L.; Wang, Y. Synthesis of monoclinic structured BiVO$_4$ spindly microtubes in deep eutectic solvent and their application for dye degradation. *J. Hazard. Mater.* **2010**, *181*, 1102–1108. [CrossRef]

18.　Huang, C.; Hu, J.; Cong, S.; Zhao, Z.; Qiu, X. Hierarchical BiOCl microflowers with improved visible-light-driven photocatalytic activity by Fe(III) modification. *Appl. Catal. B* **2015**, *174*, 105–112. [CrossRef]

19.　Lopes, O.F.; Carvalho, K.T.; Nogueira, A.E.; Avansi, W.; Ribeiro, C. Controlled synthesis of BiVO$_4$ photocatalysts:Evidence of the role of heterojunctions in their catalytic performance driven by visible-light. *Appl. Catal. B Environ.* **2016**, *188*, 87–97. [CrossRef]

20.　Cooper, E.R.; Andrews, C.D.; Wheatley, P.S.; Webb, P.; Wormald, P.; Morris, R. Ionic liquids and eutectic mixtures as solvent and template in synthesis of zeolite analogues. *Nature* **2004**, *430*, 1012–1016. [CrossRef]

21.　Liu, C.; Zhou, J.; Su, J.; Guo, L. Turning the unwanted surface bismuth enrichment to favourable BiVO$_4$/BiOCl heterojunction for enhanced photoelectrochemical performance. *Appl. Catal. B Environ.* **2019**, *241*, 506–513. [CrossRef]

22.　Su, Q.; Zhu, L.; Zhang, M.; Li, Y.; Liu, S.; Lin, J.; Song, F.; Zhang, W.; Zhu, S.; Pan, J. Construction of a Bioinspired Hierarchical BiVO$_4$/BiOCl Heterojunction and Its Enhanced Photocatalytic Activity for Phenol Degradation. *ACS Appl. Mater. Interfaces* **2021**, *13*, 32906–32915. [CrossRef] [PubMed]

23.　Zhang, D.; Wu, Z.; Zong, X. Metal-organic frameworks-derived zinc oxide nanopolyhedra/S,N: Graphene quantum dots/polyaniline ternary nanohybrid for high-performance acetone sensing. *Sens. Actuators B Chem.* **2019**, *288*, 232–242. [CrossRef]

24.　Shan, L.; Liu, Y.; Suriyaprakash, J.; Ma, C.; Wu, Z.; Dong, L.; Liu, L. Highly efficient photocatalytic activities, band alignment of BiVO$_4$/BiOCl {001} prepared by in situ chemical transformation. *J. Mol. Catal. A Chem.* **2016**, *411*, 179–187. [CrossRef]

25.　Ma, X.; Ma, Z.; Liao, T.; Liu, X.; Zhang, Y.; Li, L.; Li, W.; Hou, B. Preparation of BiVO$_4$/BiOCl heterojunction photocatalyst by in-situ transformation method for norfloxacin photocatalytic degradation. *J. Alloys Compd.* **2017**, *702*, 68–74. [CrossRef]

26.　Mahyari, M.; Bide, Y.; Gavgani, J.N. Iron(III) porphyrin supported on S and N co-doped graphene quantum dot as an efficient photocatalyst for aerobic oxidation of alcohols under visible light irradiation. *Appl. Catal. A Gen.* **2016**, *517*, 100–109. [CrossRef]

27.　Liu, B.; Yan, X.; Yan, H.; Yao, Y.; Cai, Y.; Wei, J.; Chen, S.; Xu, X.; Li, L. Preparation and characterization of Mo doped in BiVO$_4$ with enhanced photocatalytic properties. *Materials* **2017**, *10*, 976. [CrossRef]

28. Majid, M.-F.; Ghorbani, F.; Mosleh, N. Boric acid modified S and N co-doped graphene quantum dots as simple and inexpensive turn-on fluorescent nanosensor for quantification of glucose. *Spectrochim. Acta Part A Mol. Biomol. Spectrosc.* **2021**, *245*, 118892.

29. Moral-Rodríguez, A.I.; Quintana, M.; Ramos, R.L.; Galvan, H.J.O.; Oros-Ruiz, S.; Peralta, R.; Mendoza-Mendoza, E. Novel and green synthesis of BiVO4 and GO/BiVO4 photocatalysts for efficient dyes degradation under blue LED illumination. *Ceram. Int.* **2022**, *48*, 1264–1276. [CrossRef]

30. Hu, Y.; Li, D.; Sun, F.; Wang, H.; Weng, Y.; Xiong, W.; Shao, Y. One-pot template-free synthesis of heterophase $BiVO_4$ microspheres with enhanced photocatalytic activity. *RSC Adv.* **2015**, *5*, 54882–54889. [CrossRef]

31. Huang, J.; Lai, M.; Yang, J.; Wang, W.; Xu, C.; Zheng, G.; Xu, L.; Yao, S.; Wang, X.; Ma, Y. Surface decoration of BiOCl with $BiVO_4$ particles towards enhanced visible-light-driven photocatalytic performance. *Mater. Res. Express* **2019**, *6*, 045512. [CrossRef]

32. Li, H.; Chen, Y.; Zhou, W.; Jiang, H.; Liu, H.; Chen, X.; Guohui, T. WO_3/$BiVO_4$/BiOCl porous nanosheet composites from a biomass template for photocatalytic organic pollutant degradation. *J. Alloys Compd.* **2019**, *802*, 76–85. [CrossRef]

33. Hu, Y.; Li, D.; Wang, H.; Zeng, G.; Li, X.; Shao, Y. Role of active oxygen species in the liquid-phase photocatalytic degradation of RhB using $BiVO_4$/TiO_2 heterostructure under visible light irradiation. *J. Mol. Catal. A Chem.* **2015**, *408*, 172–178. [CrossRef]

34. Lv, D.; Zhang, D.; Pu, X.; Kong, D.; Lu, Z.; Shao, X.; Ma, H.; Dou, J. One-pot combustion synthesis of $BiVO_4$/BiOCl composites with enhanced visible-light photocatalytic properties. *Sep. Purif. Technol.* **2017**, *174*, 97–103. [CrossRef]

35. Abid, H.N.; Al-keisy, A.; Duha, S. Duha Constructing p-2D/n-2D BiOCl/$BiVO_4$ nanoheterostructure for photocatalytic antibacterial activity: Constructing p-2D/n-2D BiOCl/$BiVO_4$ nanoheterostructure for photocatalytic antibacterial activity. *SPAST Abstr.* **2021**, *1*.

36. Saravanakumar, K.; Maheskumar, V.; Yea, Y.; Yoon, Y.; Muthuraj, V.; Park, C.M. 2D/2D nitrogen-rich graphitic carbon nitride coupled Bi_2WO_6 S-scheme heterojunction for boosting photodegradation of tetracycline: Influencing factors, intermediates, and insights into the mechanism. *Compos. Part B Eng.* **2022**, *234*, 109726. [CrossRef]

37. Jiang, R.; Wu, D.; Lu, G.; Yan, Z.; Liu, J.; Zhou, R.; Matthew, N. Fabrication of Fe_3O_4 quantum dots modified BiOCl/$BiVO_4$ p-n heterojunction to enhance photocatalytic activity for removing broad-spectrum antibiotics under visible light. *J. Taiwan Inst. Chem. Eng.* **2019**, *96*, 681–690. [CrossRef]